Orientation-Driven Chirality Funnels in Chiral Low-Dimensional Lead-Halide Perovskite Heterostructures

Shangpu Liu,* Jonathan Zerhoch, Markus W. Heindl, Chaoran Zhang, Tim Kodalle, Kun Sun, Andrii Shcherbakov, Stanislav Bodnar, Milon Miah, Mohammad Gholipoor, Christian Jandl, Alexander Pöthig, Joachim Ballmann, Ian D. Sharp, Peter Müller-Buschbaum, Carolin M. Sutter-Fella, Ulrich W. Paetzold, and Felix Deschler*

ABSTRACT: Chiral hybrid metal-halide perovskites show low-symmetry crystal structures, large Rashba splitting, spin-filtering, and strong chiroptical activity. Circular dichroism and circularly polarized photoluminescence have been investigated in chiral perovskites with increasingly distorted chiral structures. Here, we report the fabrication of chiral (*R*/*S*)-EBAPbI$_3$ (EBA = α-ethylbenzylamine) single crystals, which possess highly distorted octahedral structures with a high angle variance value of ~68 degree^2. Using control in the fabrication conditions, we transfer chiral single crystals to thin films and achieve different crystal orientation preferences that induce tunable chiroptical properties to their heterostructures with PbI$_2$ nanodomains, which we characterize with in situ X-ray diffraction and grazing-incidence wide-angle X-ray scattering measurements. Using transient chiroptical spectroscopies, we resolve photoexcited charge carrier dynamics and chirality transfer processes in such heterostructures down to cryogenic temperatures. We observe rapid carrier transfer along the in-plane (002) facets in chiral perovskite phases to PbI$_2$ nanostructures within the initial few picoseconds, while carrier transfer along the out-of-plane (002) facets occurs at a slower rate. This fast transfer process leads to high photoluminescence intensities and large degrees of circular polarization in the emission from PbI$_2$ nanodomains at cryogenic temperatures. Our findings report a multidimensional chiral-achiral heterostructure which takes advantage of controllable chirality transfer and offers new routes for future spintronic and chiroptical applications.

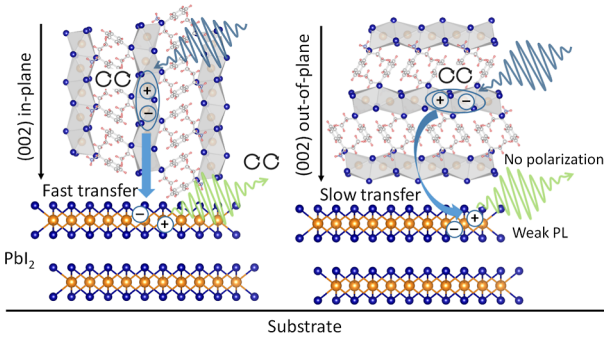

INTRODUCTION

Hybrid metal-halide perovskites have shown great potential for future optoelectronic devices, including light-emitting diodes,[1,2] photodetectors,[3,4] solar cells,[5] and lasers,[6] due to their excellent emission quantum efficiencies, promising charge-transport properties, and strong defect tolerance. By changing the organic components and inorganic elements, hybrid perovskite materials offer diverse opportunities for tailoring crystal structures, band edge electronic structures, and resulting optical properties. Indeed, owing to their tunable composition, variable bandgaps, and strong spin−orbit coupling, hybrid perovskites are of particular interest for multifunctional applications, such as for polarized light generation and detection,[7−11] second harmonic generation,[12] piezoelectrics,[13,14] and spintronics.[15,16] It has been reported that, by embedding chiral organic molecules into hybrid perovskites, distorted low-symmetry perovskite crystal structures can be achieved. The resulting chiral perovskites belong to Sohncke space groups.[17,18] These materials frequently exhibit promising chiroptical features due to their chiral crystal structures and broken inversion symmetry.[17,19]

Two main routes can be exploited for the formation of chiral perovskites. One route is to use chiral organic molecules as ligands to create chiral perovskite nanocrystals,[20−22] which tend to exhibit high PL intensities due to quantum confinement, but relatively low degrees of chiroptical polarization and limited stability. Another route is using chiral organic cations within the material itself to form chiral perovskite crystal structures.[17−19] However, the introduction of chirality into perovskite structures leads to the formation of low-dimensional perovskites because of the large chiral organic groups that are required, which decrease their conductivity and often also photoluminescence quantum efficiency (PLQE) due to increased trap state concentrations and strong electron−

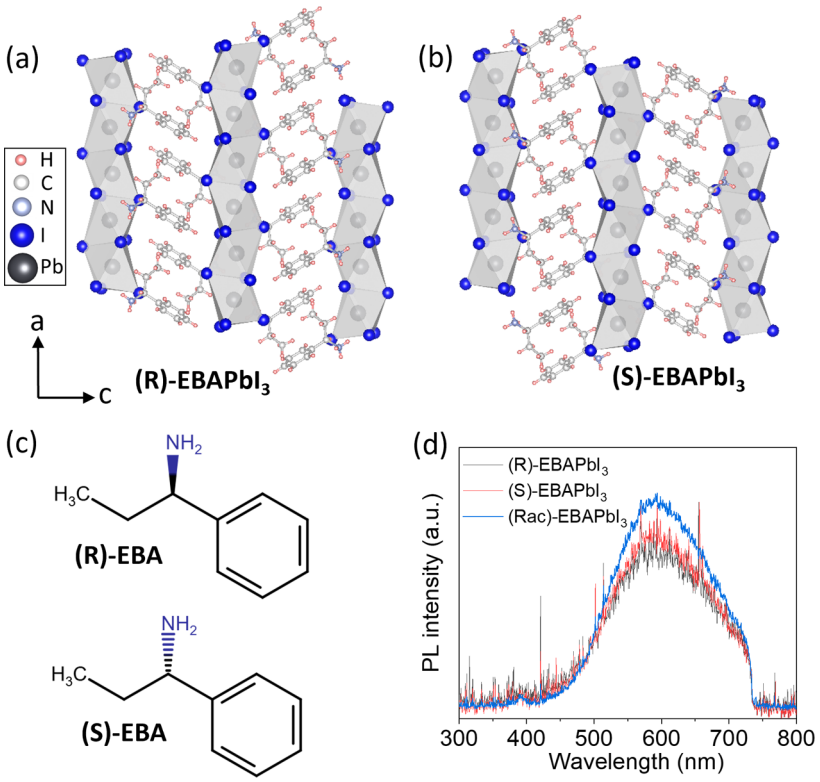

Figure 1. Structural and luminescence characterization of chiral 1D (*R*/*S*/Rac)-EBAPbI$_3$ perovskite single crystals. (a,b) Structure of (*R*/*S*)-EBAPbI$_3$ from single-crystal X-ray diffraction. (c) Chemical structures of chiral organic enantiomers (R/S)-EBA. (d) Room-temperature PL spectra collected from chiral (*R*/*S*/Rac)-EBAPbI$_3$ single crystals.

phonon coupling.[9,23] Recently, low-dimensional chiral hybrid perovskites with high PLQE at room temperature have been reported.[9] Notably, chiral two-dimensional (2D) layered perovskites are well-known for their high degree of circularly polarized photoluminescence (CPL) polarization in their single crystal or exfoliated forms.[7,9,14] However, the degree of CPL polarization for thin film samples remains in the low percentage range.[8,24] Additionally, most reported work about chiral one-dimensional (1D) chain perovskites focuses on their strong circular dichroism (CD) signals, which can be utilized for circularly polarized light detection.[3,4] However, due to their disconnected face-sharing octahedral chains, chiral 1D perovskites show weak PL intensities at room temperature, and only very low CPL was reported from chiral 1D perovskites, which prevents their use for optoelectronic applications.

Chiral 1D perovskites can differentially absorb circularly polarized light, but not efficiently emit light.[19,25] Here, we report a simple solution-processed method for fabricating chiral perovskite/PbI$_2$ heterostructure thin films wherein the chiral properties of chiral perovskite are effectively transferred to PbI$_2$ nanostructures. The resulting heterostructures exhibit broad CD signals, covering the spectral range of 300−550 nm, with a degree of CPL polarization of ∼4% at low temperatures. In addition, we show that solvent engineering promotes chiral perovskite/PbI$_2$ heterostructure formation. Using single crystal X-ray diffraction (SCXRD) of bulk materials, in situ XRD during subsequent film synthesis, and grazing incident wide-angle X-ray scattering (GIWAXS) of the fabricated films, we analyze in situ spin-coated thin films and relate fast carrier funnels to preferential crystal orientations within chiral perovskite/PbI$_2$ thin films. We further investigate the carrier and chirality transfer dynamics in chiral perovskite heterostructures by transient chiroptical spectroscopy and rationalize the enhanced angular momentum polarization lifetime and CPL to arise from fast and effective carrier transfer from the chiral perovskite phase to PbI$_2$ heterostructures. Our findings indicate the potential of solution-processed chiral perovskite heterostructure thin films for future optoelectronic and spintronic applications.

RESULTS AND DISCUSSION

Structural and Emission Characteristics of Chiral 1D Perovskite Crystals. We prepared chiral 1D perovskite (*R*/*S*/Rac)-EBAPbI$_3$ single crystals by slow cooling. The same single crystal structures were also reported before.[26] In brief, after fully dissolving (*R*/*S*/Rac)-EBA and PbO in HI solution at 95 °C, we controllably cooled the reaction vessel down to room temperature at a rate of ∼1 °C/h. During cooling, large needle-shaped single crystals formed gradually (Figure S1). SCXRD measurements were used to identify the crystal structures of the resulting chiral perovskites (see detailed crystal structure results in Table S1), which comprise 1D chains of distorted face-sharing PbI$_3$ octahedra surrounded by alternating chiral organic molecules (Figure 1a−c). Chiral (*R*) and (*S*) 1D perovskite samples have a similar mirror-like crystal structure, both crystallizing in an orthorhombic $P2_12_12_1$ space group, which belongs to one of the Sohncke space groups[17] and confirming successful chirality transfer from chiral organics to the inorganic lead halide chains.

SCXRD analysis reveals a prominent structure distortion in our chiral 1D perovskites. Both chiral (*R*) and (*S*) single crystals show varied Pb−I bond distances from 3.08 to 3.43 Å, with a similar octahedral bond length distortion index of 0.027 (detailed calculations in Table S2), which should be zero for a

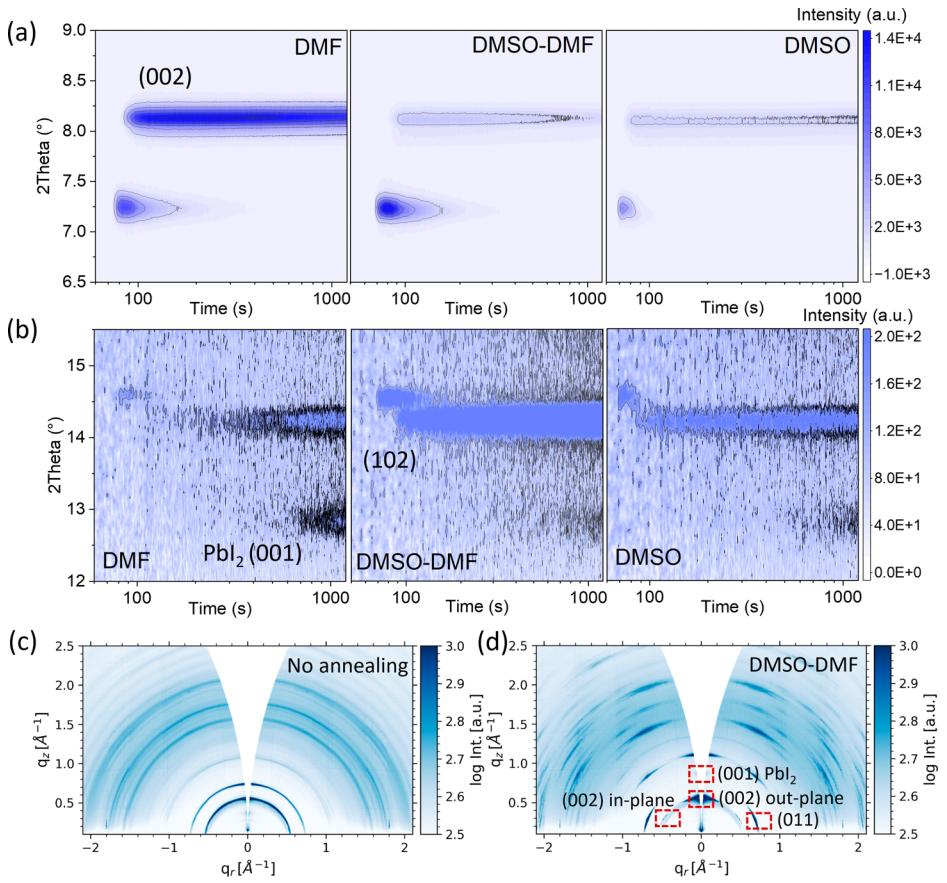

Figure 2. Structural evolution of chiral 1D (*R*)-EBAPbI$_3$/PbI$_2$ thin films during spin-coating. (a,b) In situ XRD maps of chiral perovskite/PbI$_2$ thin films monitored during spin-coating (before 60 s) and during the subsequent annealing process at 100 °C (after 60 s). The films were fabricated using three different solvents, DMF, DMSO, and a 1:1 DMF-DMSO mixture. The XRD patterns are expanded in two different regions, 6.5 to 9.0° (a), and 12.0 to 15.5° (b). (c,d) 2D GIWAXS data for perovskite films fabricated using a 1:1 DMSO−DMF mixture (c) without and (d) with a 10 min annealing process at 100 °C.

perfect octahedron with full symmetry. Importantly, a much higher angle variance value of ~ 68°[2] is observed for our chiral 1D perovskites, which is among the highest values of the so far reported chiral perovskite semiconductors,[27] indicating the strongly broken symmetry in our chiral 1D perovskites. Besides, we find chiral 1D perovskite (*R*), (*S*), and (Rac)-EBAPbI$_3$ crystals all exhibit broad-band emissions at sub-band positions (400−750 nm, Figure 1c). We attribute such broad-band emission to the trapped excitons, which have been widely reported in low dimensional perovskites.[28−30] There is no obvious free exciton PL signal observed in our chiral 1D perovskite single crystals, similar to other 1D perovskites,[4,25] which may hinder their chiroptical applications. However, we hypothesize that the strong chirality present in our chiral 1D perovskite crystal structures, which can be also used for efficient polarized carrier injections, beyond the limit of pure phase chiral materials.

Fabrication of Chiral Perovskite/PbI$_2$ Heterostructures. For compatibility with optoelectronic applications, we next converted single-crystal samples to polycrystalline thin films using a simple solution-based spin-coating method (see details in Materials and Methods section). Thin film fabrication yields heterostructures of chiral 1D perovskites and PbI$_2$ nanodomains, as we will show in the following. We used three different solvents (DMF, DMSO, and a mixture of DMSO and DMF in equal volumes) to dissolve perovskite single crystals and studied how the solvents impact the film structure and morphology. The obtained precursor solutions were directly spin-coated on glass substrates that were precleaned with oxygen plasma. The corresponding samples are henceforth denoted as DMF, DMSO, and DMSO−DMF films. The same solvent engineering methods were used to control the CPL of chiral 2D perovskite/QDs compositions.[31]

To directly monitor the crystallization of the perovskite films, we performed in situ XRD measurements. As depicted in Figure 2a,b, as well as the extended range in situ XRD results shown in Figure S2, no obvious diffraction signal is observed within the initial 60 s, which includes the complete spin-coating process. However, once thermal annealing (100 °C) was initiated at 60 s, a transient intermediate state, characterized by a diffraction peak at 7.3°, emerged, which subsequently gradually diminished and vanished after ~300 s for DMF and DMSO−DMF films, but more quickly (~100 s) for the pure DMSO film. Importantly, the (002) reflection from the chiral 1D perovskites, located at 8.2°, appeared at ~100 s and then remained stable through the end of the experiment. Much stronger (002) diffraction intensities were observed in the DMF films compared to the other two films, as discussed below. In addition, a reflection located at 14.3° appeared after 100 s for DMSO−DMF film, while this signal was weaker for the DMSO film, and much weaker for the pure DMF film. Compared to simulated patterns derived from both chiral perovskite and PbI$_2$ single crystal structures (Figure S3), we attribute this new reflection pattern to the (102) facet of

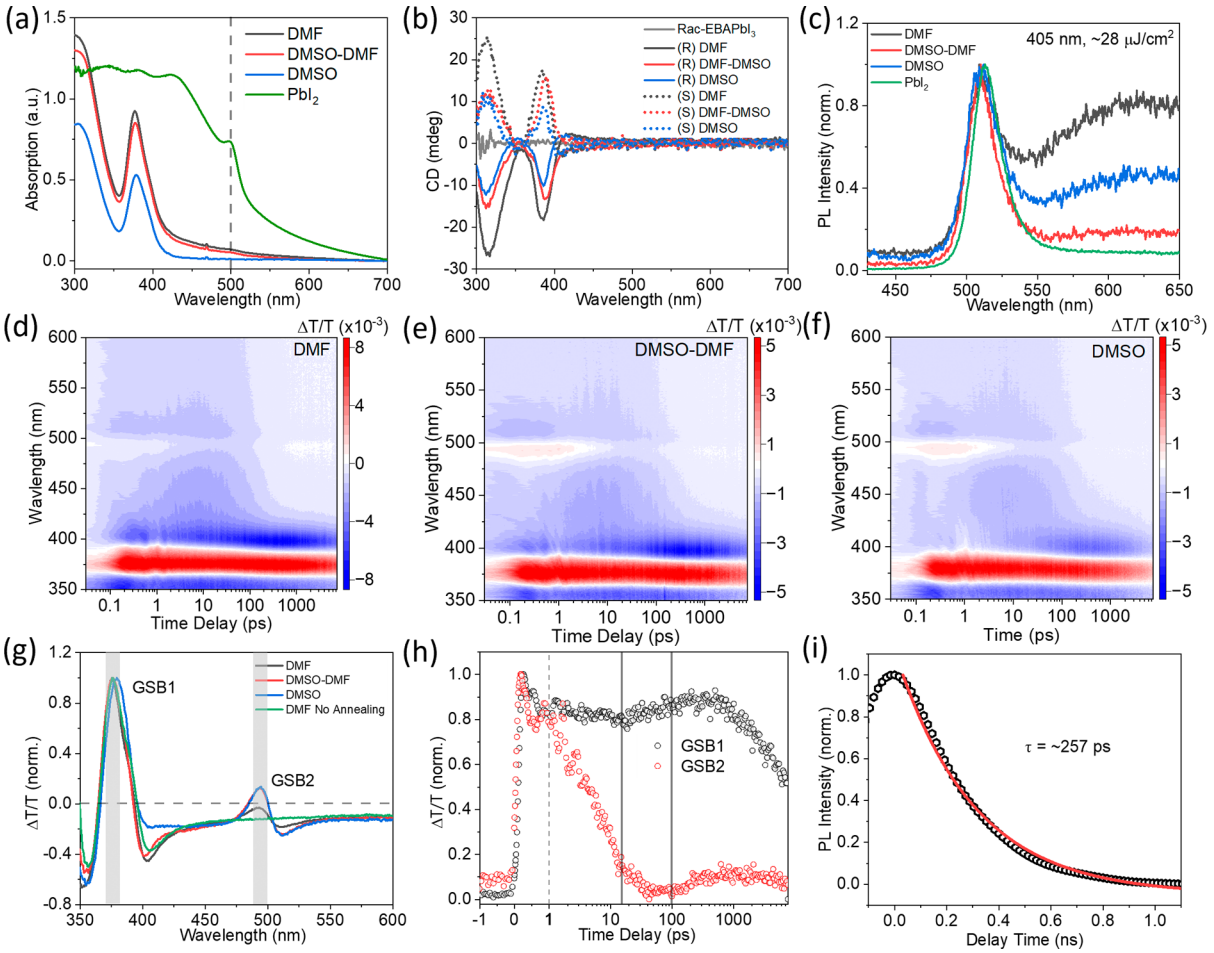

Figure 3. Excited state dynamics in chiral (*R*)-EBAPbI$_3$/PbI$_2$ thin films. (a) Steady-state room-temperature UV−vis absorption, (b) circular dichroism, and (c) PL spectra of the studied chiral perovskite thin films. (d−f) Transient absorption (pump wavelength 340 nm, fluence ∼180 μJ/cm^2) color maps of chiral perovskite thin films fabricated using DMF (d), mixed DMSO−DMF (e), and DMSO solvents (f). (g) Comparison of TA spectra averaged over the initial 1 ps after excitation of films prepared from different solvents. The thin films were annealed at 100 °C for 10 min. For comparison, DMF-derived films were fabricated without annealing. Gray regions indicate spectral regions of two GSB signals. (h) TA kinetics extracted from the two GSB regions highlighted in (g) for the annealed DMF-derived film. The GSB2 kinetics were corrected for the underlying broad photoinduced absorption by subtracting the signal in the range 550−560 nm. Gray lines indicate the time delay at which the rise starts in GSB1 and GSB2 signals, respectively. (i) TCSPC kinetics of the annealed DMF-derived film, obtained at a luminescence detection wavelength of 505 nm (excitation wavelength 405 nm, fluence of ∼10 μJ/cm^2).

chiral 1D perovskite phases. Besides, PbI$_2$ phases located at 12.7° emerge in all three films after 10 min annealing process (Figures 2b and S3). In summary, the chiral 1D perovskite films show similar characteristics, though with a dominant (002) reflection due to the thin film texture, and PbI$_2$ signals were observed in all three samples, indicating the formation of chiral perovskite/PbI$_2$ heterostructures. Solvent engineering is a general method for controlling the formation of perovskite films due to the different solubilities of selected solvents.[32−34] Similar in our work, the formation of PbI$_2$ (DMSO) intermediate has been reported as an important factor to get high-quality perovskite films.[35] Besides, we observed the formation of PbI$_2$ during the 100 °C annealing process. The different evaporation temperatures of the used solvents (DMSO or DMF), and differences in solubility of (*R*/*S*)-EBA, PbI$_2$ and (*R*-/*S*)-EBAPbI$_3$ further influence the growth process of PbI$_2$ phases. We note that there is a rather broad background signal at higher angles for the DMSO and DMSO−DMF samples that is not present for the DMF sample. This may relate to the presence of an amorphous or highly disordered phase, potentially due to residual DMSO.

To further investigate the crystal orientations within chiral perovskite films, we performed GIWAXS measurements using synchrotron radiation. For the spin-coated perovskite films without subsequent thermal annealing (Figure 2c), smooth diffraction rings are observed, indicating highly randomized distributions of the crystal orientations within the polycrystalline perovskite films. However, for the perovskite films that were thermally annealed at 100 °C for 10 min after spin coating (Figures 2d and S4), we observe several intense Bragg spots within each ring, which indicates preferential crystal orientations in the films. Out-of-plane PbI$_2$ (001) reflection appears in all three films after annealing process (Figure S4). Besides, the dominant (002) reflection in chiral perovskite phases corresponds to the preferred out-of-plane orientation for all three types of films. However, for DMSO−DMF and DMSO films, we observe an additional in-plane (002) contribution. Thus, the mixed orientations within these films may explain the weaker (002) reflection intensities observed during in situ XRD measurements (Figure 2a). Alongside the (002) reflection, an in-plane (011) contribution is observed for the DMF films. For DMSO−DMF films, the detection of

smooth diffraction rings indicates a random orientation of (011) planes (Figure S4).

Overall, our GIWAXS measurements indicate that the solvents used during the spin-coating process influence the crystal orientations within the perovskite films, similar to recently reported work,[36] which uses Cl substitutes to vary film growth orientations. The (002) orientation along the out-of-plane direction is dominant in DMF films, while DMSO−DMF and DMSO films contain some material with in-plane or random (002)/(011) orientations. Similar trends are also found in atomic force microscope (AFM) measurements, in which different solvents lead to different surface morphologies, which may also relate to their thin film textures (Figure S5). As expected, DMF films with one dominant lattice orientation show uniform film surface morphology, while mixtures of different lattice orientations in DMSO−DMF and DMSO films result in more corrugated film surface morphology (Figure S6).

General Optical Characteristics of Chiral Perovskite/PbI_2 Films. Considering the interesting chiral structures of these 1D perovskite films and their solvent-tunable morphologies, we now study their optical properties. Steady-state absorption spectra show that our chiral perovskite films exhibit an excitonic absorption peak at ∼378 nm for all three solvents (Figure 3a), which indicates a band gap that is similar to the reported 1D perovskites.[4,25,29] Next, we used a Mueller matrix model to obtain the chiroptical signals.[37−39] Specifically, we rotated and flipped the samples to record contributions from linear dichroism (LD) or linear birefringence (LB). The results show no stark changes in CD signals during rotations, confirming weak contributions from LD and LB. However, large differences were observed in all three films when we flipped the samples (Figure S7), which indicates the contributions from oriented LB and LD axes (LBLD). Such LB and LD contributions are strongly related to the film textures and morphologies (Figure S5). To obtain pure CD signals, we average the signals obtained from film flipping, following standard protocols.[39] Figure 3b presents the intrinsic CD results from the chiral 1D (*R*)-EBAPbI$_3$ perovskite films. Opposite CD signals are observed for (*R*/*S*)-EBAPbI$_3$ films, while no CD signals are found in racemic EBAPbI$_3$ films. Importantly, the main CD signals from chiral perovskite films are located at the absorption band positions (∼378 nm), demonstrating chirality transfer from the chiral organic molecules to the metal-halide moieties. The same result is also obtained from analysis of the absorption anisotropy factors (g_{abs}) (see detailed calculations in Figure S8), which are independent of film thickness and absorption intensities.[17,40,41] Importantly, we find that different solvents resulted in pronounced changes to the CD signals. Perovskite films formed from DMF solvents show the largest CD signal, with a g_{abs} value of ∼0.001 at band edge position. The chiroptical features in chiral perovskites are strongly related to their crystal symmetry and Rashba splitting at band edges.[42] Thus, in our current work, by changing the spin-coating solvents, we reach different crystal orientations in chiral perovskite films. More ordered structures would lead to less strain in the crystal lattice, so that chiral effects are more clearly seen in the CD, similar work is also reported before.[43]

Next, we study the PL of our chiral 1D perovskite films. Under 340 nm excitation, no PL signal is observed at the band edge (∼378 nm) for any of the films, regardless of the solvent used for their preparation (Figure S9). This observation is reasonable, considering that most reported chiral 1D perovskites do not exhibit band edge PL due to indirect band structures.[4,25] Notably, a weak subgap PL band appears at ∼510 nm in our chiral perovskite films (Figure 3c), along with a broad PL feature located from 550 to 650 nm that we attribute to a trapped exciton, consistent with what we find before from single crystals (Figure 1c).[23] Using different solvents changes the intensity of this trapped-exciton PL signal, with the highest intensities in DMF films and lowest intensities in DMSO−DMF films. However, the origin of the PL peak at 510 nm is less clear. To identify this feature, we prepare pure PbI_2 thin films using identical spin-coating conditions (40 mg PbI_2 dissolved in 200 μL DMSO−DMF solutions), which show a yellowish color compared to transparent chiral 1D perovskite films (Figure S10). The pure PbI_2 films show a PL feature at ∼510 nm (Figure 3c), which has been widely reported before.[44,45] We further compared the absorption spectra between pure PbI_2, (*R*)-EBAPbI$_3$, and (*R*)-EBAPbI$_3$ films with excess PbI_2 added into the spin-coating solution. We find that both PbI_2 and (*R*)-EBAPbI$_3$ films with excess PbI_2 show a noticeable absorption band feature at 500 nm, which overlaps well with the shoulder in the absorption signals of pristine (*R*)-EBAPbI$_3$ films (Figures 3a and S11a). In addition, XRD and GIWAXS measurements indicate the presence of PbI_2 phases in chiral perovskite films (Figures 2, S4 and S11b). Cross-sectional SEM image confirmed there is no bilayer heterojunction formation in the spin-coated chiral perovskite films (Figure S12). From surface EDX mapping (Figure S13), no aggregation is detected in the films, indicating dispersed PbI_2 nanodomains in chiral 1D perovskites. Thus, we conclude that the 500 nm feature in (S/R)-EBAPbI$_3$ films originates from a chiral perovskite/PbI_2 mixed, bulk heterostructure comprising well-dispersed PbI_2 phases.[46] Recent studies have reported that the addition of large organic precursors in perovskite spin-coating solutions results in on-substrate formation of perovskite nanostructures with sizes from hundreds of nm to a few nm.[2,47−49] Such ligand engineering methods provide a new strategy for the in situ fabrication of perovskite nanocrystal thin films during the spin-coating process. Accordingly, in our work, during spin-coating process, we think most of (*R*/*S*)-EBAI was bonded with PbI_2 to form a chiral 1D perovskite bulk phase, while the rest (*R*/*S*)-EBA may confine the growth of PbI_2, leading to the formation of PI_2 nanostructured phases with (*R*/*S*)-EBA acting as surface ligands. In our work, upon dissolving the single crystals prior to spin-coating, differences in solubility of (*R*/*S*)-EBA, PbI_2, and (*R*-/*S*-EBAPbI$_3$) will lead to an equilibrium of these chemical phases in the solution. We also add additional (*R*)-EBAI precursor (20 mg) in spin-coating solutions to prepare (*R*)-EBAPbI$_3$ films, the 500 nm absorption shoulder disappears, which may be due to the consumption of all PbI_2 in the films to form chiral 1D perovskites (Figure S14). We further add 40 mg of (*R*)-EBAI in the precursor solutions. We find that too much access amount of chiral organic molecules (4-fold) compared to the PbI_2 precursors may suppress the formation of the 1D perovskite phase and dilute the concentration of perovskites in the films, resulting in the disappearance of (*R*)-EBAPbI$_3$ absorption peak. To estimate the content of PbI_2 phases in the films, we compared the absorption intensities (*A*) of pure PbI_2 films (0.40 mmol/mL, *A* = ∼0.73) with chiral perovskite/PbI_2 films (DMSO−DMF) at 500 nm (*A* = ∼0.06) (Figure 3a), in which pure phase 1D perovskites (0.25 mmol/mL) show no absorption. From this

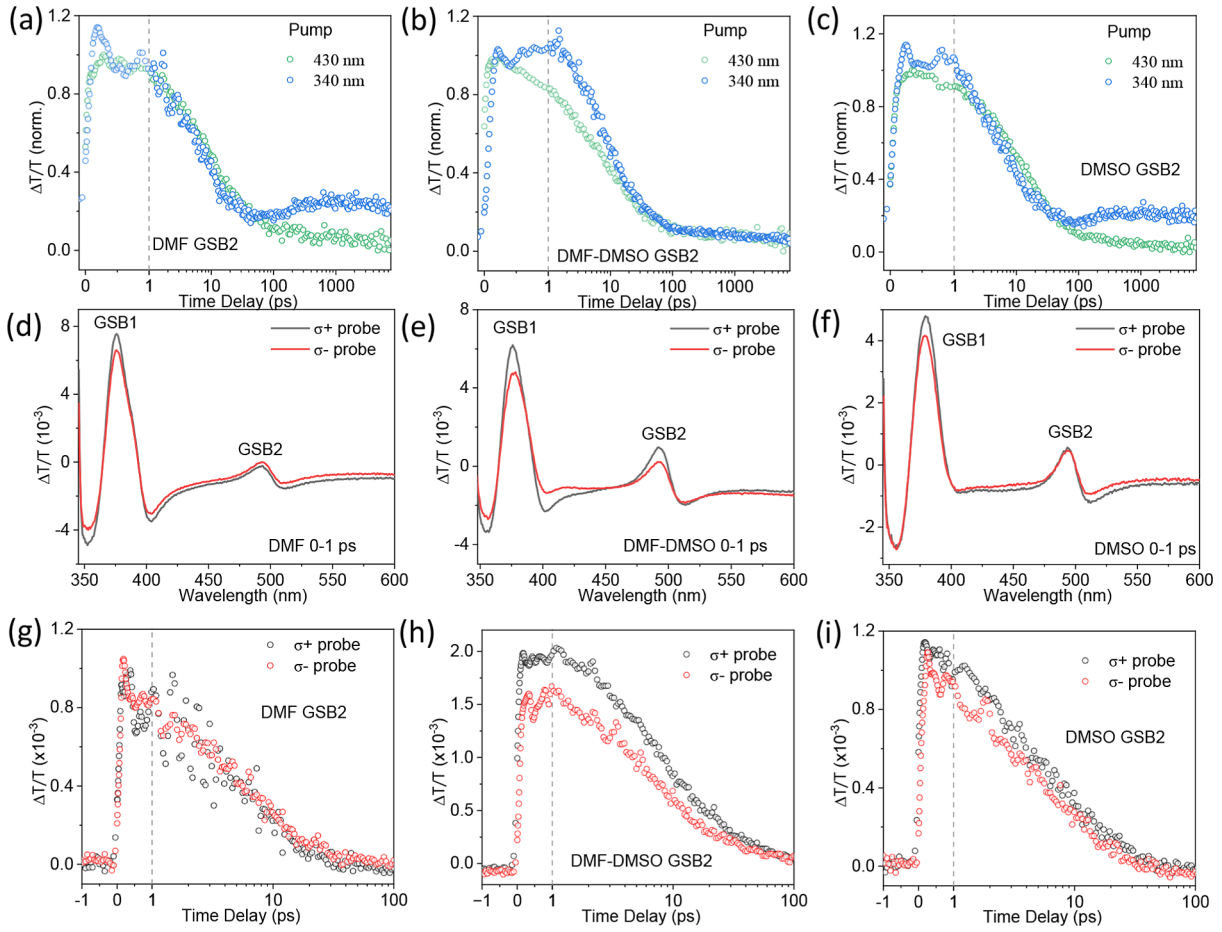

Figure 4. Photoexcited state polarization dynamics in chiral (*R*)-EBAPbI$_3$/PbI$_2$ thin films. (a–c) Comparison of linear TA kinetics at GSB2 regions under excitations at 340 and 430 nm, respectively. The TA kinetics were obtained from (a) DMF, (b) DMSO–DMF, and (c) DMSO films. (d–f) CTA spectra in the initial 1 ps after excitation for chiral perovskite thin films deposited using (d) DMF, (e) DMF–DMSO, and (f) DMSO. A linearly polarized 340 nm (~180 μJ/cm^2) pump was used to excite each of the samples. Circularly polarized right-handed (σ^+) and left-handed (σ^-) probes were used to detect TA signals. (g–i) CTA kinetics at initial 100 ps collected from GSB2 regions from panels in Figure 4d–f, respectively. CTA kinetics to the nanosecond regime are shown in Figure S18.

analysis, the resulting PbI$_2$ molar content is ~13% relative to the chiral perovskite phases in the films.

To study the mechanism behind the formation of the ~510 nm PL feature from the PbI$_2$ nanodomains, we performed transient absorption (TA) spectroscopy measurements on our chiral 1D perovskite/PbI$_2$ heterostructures (Figure 3d–f). Two ground-state bleach (GSB) signals were observed from TA spectroscopy. One feature (GSB1), located at ~378 nm, originates from the 1D perovskite band edge, while a second bleach signal (GSB2) at ~495 nm corresponds to the ~510 nm PL feature with a Stokes shift of ~15 nm.[50] For reference, we also prepared one chiral perovskite sample using DMF as a solvent but without subsequent thermal annealing. The corresponding TA spectrum from this reference sample reveals that no GSB2 feature is present, suggesting that the associated perovskite/PbI$_2$ heterostructure is not formed in the absence of annealing (Figure 3g). In contrast, the GSB2 feature is present for pure PbI$_2$ films and all studied chiral 1D perovskite/PbI$_2$ heterostructures and following the 10 min thermal annealing process (Figure S15). However, the solvent strongly influences this signal's magnitude, with both DMSO–DMF and DMSO films exhibiting a stronger GSB2 TA signal than the DMF films. Interestingly, GIWAXS and in situ XRD measurements revealed a similar dependence on the strength of the (002) reflection with solvent (Figure S3) and with the annealing routine (Figure 2). Hence, the GSB2 signals observed in chiral perovskite samples appear to be correlated with the presence of (002) oriented in-plane domains, which may promote chiral perovskite/PbI$_2$ heterostructure formation.

TA kinetics further revealed that GSB1 has a much longer lifetime than GSB2 (Figure 3h). Inspection of the kinetic traces indicates that the GSB2 feature initially decays quickly (within the first 10 ps), which is consistent with relaxation of states that were directly populated by the photoexcitation. However, the signal recovers after hundreds of picoseconds, corresponding to the time scale on which the GSB1 kinetics change and start to decay more rapidly. Such a behavior points toward excitation transfer from GSB1 to GSB2 after ~100 ps. A rise occurs in the GSB1 signal at ~15 ps, which we attribute to carrier relaxation processes. Similar trends were also evident at PIA regions from 400 to 425 nm (Figure 3d). Time-correlated single-photon counting (TCSPC) measurements were also used to characterize the kinetics of the 510 nm PL feature. The dominant signals from trapped excitations in chiral perovskite phases are located at ~625 nm, which has very little spectral overlap with the probed PL feature. The resulting kinetics was fitted well with a monoexponential decay, which yielded a PL lifetime of ~257 ps (Figure 3i). No transfer

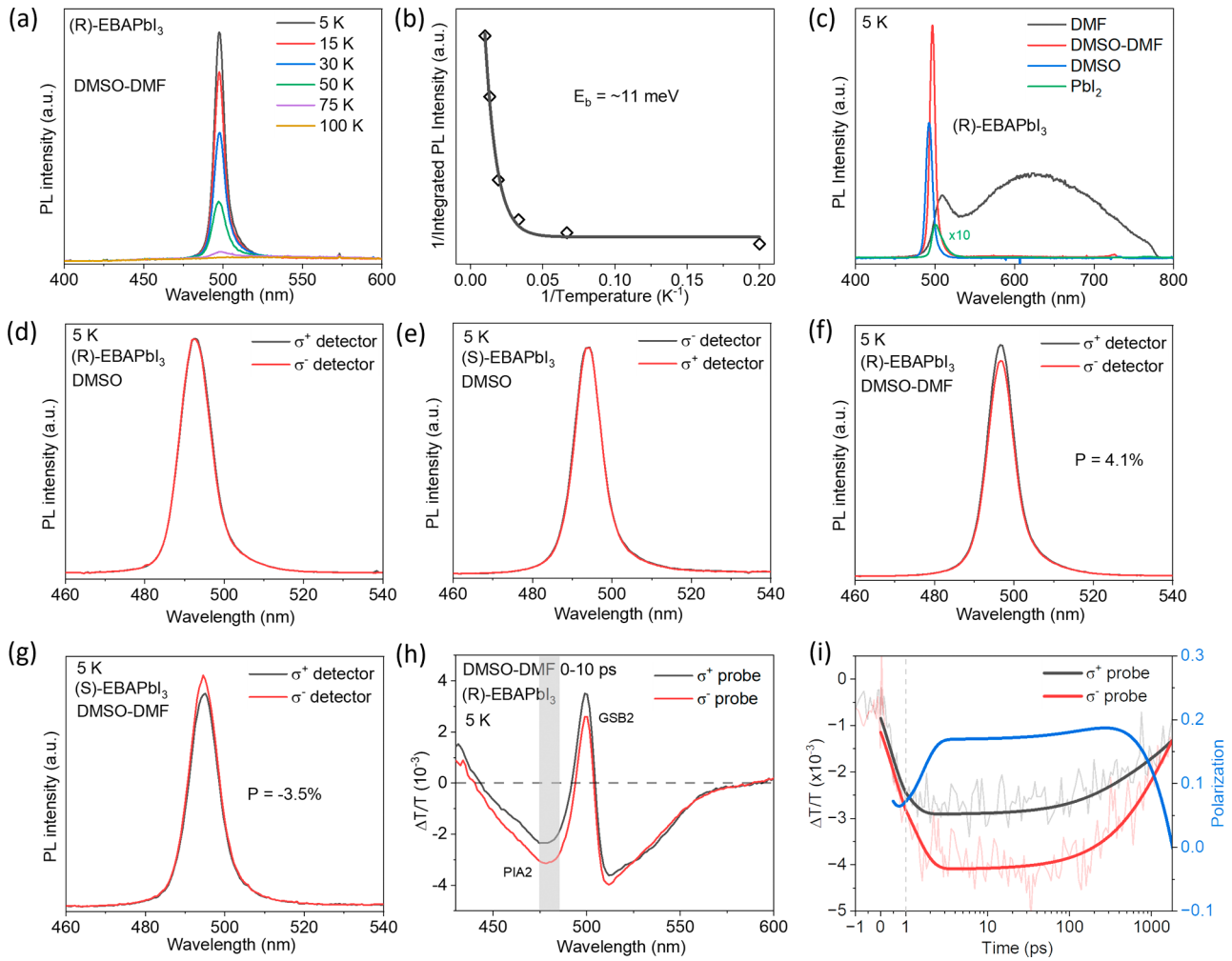

Figure 5. Chiroptical photophysics characterization of chiral perovskite/PbI_2 thin films at cryogenic temperatures. (a,b) Temperature-dependent PL spectra (a), and corresponding integrated PL intensity (b) as a function of temperature for chiral perovskite films deposited with DMSO−DMF. The samples were excited at 395 nm with a pump fluence of ~5 $\mu J/cm^2$. (c) Comparison of low temperature (5 K) PL spectra of pure PbI_2 and chiral perovskite/PbI_2 heterostructures films deposited using DMF, mixed DMSO−DMF, and DMSO solutions. (d−g) Low-temperature (5 K) CPL spectra of chiral perovskite/PbI_2 films produced using (d,e) DMSO, and (f,g) mixed DMSO−DMF. (h,i) Low temperature (5 K) CTA spectra (h) and kinetics (i) of chiral perovskite films produced using DMSO−DMF. The CTA kinetics were collected from the PIA signals, as indicated by the gray region in (h). The samples were excited at 390 nm with a pump fluence of ~14 $\mu J/cm^2$.

process was detected in the TCSPC measurements, which may be due to its limited time resolution or the transfer process mainly occurring via dark states that can only be detected in TA measurements.[51,52] However, such a longer PL lifetime (GSB2 lifetime <100 ps) further suggests the delayed population of the GSB2 transferred from a higher state (GSB1).

Room-Temperature Excited State Polarization Dynamics. To further study the chirality transfer process in our chiral perovskite heterostructures, we next compared TA data obtained using two different pump wavelengths to excite the chiral perovskite/PbI_2 films. Under 340 nm excitation, both GSB1 at ~378 nm and GSB2 at ~495 nm are excited, followed by excited state transfer from GSB1 to GSB2, which complicates the relaxation kinetics. However, we can also selectively obtain GSB2 signals under 430 nm excitations. In this case, no broad and long-lived PIA signals appeared together alongside the GSB2 signals, which we can now attribute to transitions from GSB1 to higher-lying states (Figure S16). Accordingly, there is no carrier transfer between these states under 430 nm excitation.[53] As such, a comparison of differences in the TA kinetics of the GSB2 regions obtained under 340 and 430 nm excitation enables the characterization of the carrier transfer process (Figure 4a−c). For DMF films (Figure 4a), the decay kinetics from 0.5 to 100 ps are almost overlapping for the 340 and 430 nm pumps. However, only under 340 nm excitation the TA signal again rises after ~100 ps, which confirms excited state transfer in DMF films after 100 ps. The same trends were also observed in DMSO films (Figure 4c). In contrast, for the DMF−DMSO films under 340 nm excitation (Figure 4b), the TA signal exhibits a prominent increase already within 10 ps, compared to TA signals under 430 nm excitation. These results provide a strong indication that charge carrier transfer from GSB1 to GSB2 occurs rapidly in DMF-DMSO films, while slow carrier transfer after 100 ps happens in DMSO and DMF films. Such different carrier transfer characteristics may relate to the solubility of perovskite precursors in different solvents. As widely studied in perovskite film fabrication, DMSO−DMF mixtures usually show better perovskite precursor solubility than pure DMSO or DMF solvent.[54,55] Thus, PbI_2 nanodomains are more dispersed in DMSO−DMF films, resulting in faster carrier funnels. More

importantly, based on in situ XRD and GIWAXS results, in-plane (002) facets in DMSO−DMF films offer a better carrier transport direction due to preferential alignment of 1D phase and PbI_2 nanodomains. Therefore, we conclude that carrier transfer of photoexcited electronic states occurs in our chiral 1D perovskites heterostructures which we can control by solvent engineering the film morphology and preferred orientation.

We further employed circularly polarized TA (CTA) spectroscopy to investigate the polarization dynamics of photoexcited electronic states in our chiral perovskite/PbI_2 thin films at room temperature. We use a linearly polarized pump lasers for photoexcitation, which avoids the generation of polarized populations of excited states due to circularly polarized excitations.[23] Circularly polarized broadband probe pulses were then used to study the intensity of TA signals, and intensities for left-handed and right-handed polarization of probe pulses were compared. Figure 4d−f show the CTA spectra collected for chiral perovskite/PbI_2 thin films produced using the three different solvents. All three films exhibit intensity differences in the GSB1 regions (~378 nm) for different probe pulse polarizations during the initial 1 ps, which relate to intrinsic chirality features of chiral 1D perovskites (Figure 3b). The decay kinetics extracted from GSB1 (372−382 nm) are plotted in Figure S17. Both DMF and DMSO−DMF films show a long-lived polarization lifetime (a few ns) for chiral 1D perovskite phases, while the polarization in DMSO films only lasts for ~1 ps. These long-lived polarized carriers in DMF and DMSO−DMF films are located at the band minima of chiral 1D perovskites. Potential origins of this observation are phase-dependent spin-preserving carrier scattering processes and structural asymmetries that create nondegenerate spin-textures in the band structures for oriented chiral perovskite crystals. Notably, the GSB2 feature, which we attribute to chiral perovskite/PbI_2 heterostructures, shows a non-negligible difference between right-handed (σ^+) and left-handed (σ^-) polarized probes in the DMF-DMSO film (Figure 4e), indicating successful chirality transfer from the chiral 1D perovskite phase to the PbI_2 phase. No detectable polarization of the GSB2 feature is observed for DMF and DMSO films. The minor difference between the σ^+ and σ^- detections in DMF and DMSO films are attributed to the broad photo-induced absorption (PIA) signals from chiral 1D perovskite phases extending over the range from 400 to 600 nm. Since the GSB2 signal is located on such signals, we calculated the pure GSB2 signals (490−500 nm) by subtracting the adjacent PIA signals (550−560 nm) from the raw signals at the respective GSB2 wavelengths. As shown in the resulting plots of the CTA kinetics in Figure 4g−i, after signal corrections, there is almost no difference between σ^+ and σ^- probes of the GSB2 kinetics for DMF and DMSO films, whereas DMSO−DMF films show a longer polarization lifetime reaching ~100 ps. Combined with fast carrier transfer we observed in DMSO-films (Figure 4a−c), we conclude that the strong and long-lived polarization signal in DMF-DMSO films arises from fast carrier transfer, which efficiently delivers polarized excited states from the chiral 1D perovskite phase (GSB1) to the PbI_2 heterostructure (GSB2), before depolarization occurs in the chiral 1D perovskite phase. For DMF and DMSO films, carrier transfer occurs 1 order of magnitude slower after 100 ps. At this point, the excited state population in the 1D chiral perovskite phase (GSB1) has already depolarized (Figures S17 and S18).

Low-Temperature Chiroptical Features. Given that effective chirality transfer in chiral perovskite/PbI_2 heterostructures enables long-lived polarized states, we attempted to explore the CPL properties of the chiral perovskite/PbI_2 films. However, we did not observe obvious CPL signals due to the low PL intensities from these films at room temperature. Nevertheless, PL features were detected at cryogenic temperatures. Figure 5a shows the temperature-dependent PL spectra of chiral perovskite DMSO−DMF films. A narrow PL peak at ~498 nm becomes dominant for cryogenic temperatures. This corresponds to a blue shift of the PL emission compared to room temperature (~510 nm). Additionally, the strong increase of intensity, and decrease of peak width, indicate strong electron−phonon interactions in our chiral perovskite/PbI_2 heterostructures. To quantitatively understand electron−phonon coupling in this heterostructure, we extract the integrated intensity of PL peaks from temperature-dependent PL spectra and plot them as a function of temperature (Figure 5b). In Figure 5b, the temperature dependence of the integrated PL intensity (I_{PL}) was fitted by the following equation[14]

$$I_{PL}(T) = \frac{I_0}{1 + A\exp(-E_b/k_BT)} \quad (1)$$

where E_b is the activation energy, here corresponding to the excitonic binding energy, k_B the Boltzmann constant, A a fitting constant, and I_0 the integrated intensity of the PL peak at 5 K. The fitted E_b value is only ~11 meV, which is a much smaller value than typically found in low-dimensional perovskite materials (hundreds of meV), and similar to the exciton binding energy reported in PbI_2.[56−58] Thus, this result is consistent with our conclusion that the sharp PL feature at ~500 nm originates from the PbI_2 regions of our chiral perovskite/PbI_2 heterostructures. Further, these findings explain the low PL intensity of samples at room temperature, since excitons with such a small E_b would have a high probability of thermally dissociating prior to radiatively decaying.

We now compare the PL spectra at 5 K for spin-coated chiral perovskite films prepared with different solvents (Figure 5c). The PL intensity at ~500 nm is much stronger of all chiral perovskite/PbI_2 films than that of pure PbI_2 films. Additionally, the fwhm of the PL from pure PbI_2 (~75 meV) is almost double that of chiral perovskite/PbI_2 films (~38 meV), corroborating our conclusion that the 500 nm PL feature in chiral perovskite films does not simply originate from a pure PbI_2 bulk phase. Furthermore, we hypothesize that the substantial increase in PL intensity of chiral perovskite/PbI_2 films may be due to carrier funnelling from the perovskite phase to the PbI_2 nanodomains. Consistent with this interpretation, DMSO−DMF films show a much higher PL intensity at ~500 nm than pure DMSO or DMF films, as would be expected based on the fast carrier transfer in DMSO−DMF films observed in TA spectroscopy (Figure 4a−c). This fast process can enable the efficient transfer of carriers to the PbI_2 heterostructure phase before they can recombine via nonradiative decay channels, e.g., at traps and defects.

In the DMF heterostructure films, we find a broad PL feature from 550 to 800 nm, which is similar to the PL signals from trapped excitons observed at room temperature (Figures 1 and 3c). However, at low temperatures, this peak does only appear for DMF heterostructure films. Consistent with our

other findings, this result indicates that the use of different solvents during the spin-coating process influences film crystallization, such as higher roughness in DMF films (Figure S5), leading to the formation of different types and concentrations of traps and defects.

To perform CPL measurements of chiral perovskite films at 5 K, we used linearly polarized pulses to photoexcite the samples, and a quarter waveplate (QWP), followed by a linear polarizer rotated by 45° with respect to the fast axis of the QWP, to select between σ^+ and σ^- PL signals, which were subsequently sent to the camera. Neither chiral perovskite (*R*) nor (*S*)-EBAPbI$_3$ DMSO films showed obvious PL intensity differences at ∼500 nm between σ^+ and σ^- polarizations (Figure 5d,e). This observation is consistent with their low TA polarization degrees and is a consequence of the slow carrier transfer (Figure 4a−c). We note that the dominate luminescent species in DMF films are trapped excitons rather than PbI$_2$ emissions (Figures 3c and 5c).

For DMSO−DMF films, we find clear intensity differences were detected for chiral (*R*)- and (*S*)-EBAPbI$_3$ films between σ^+ and σ^- detections (Figure 5f,g). Using these data, we calculate the degree of CPL polarization (*P*) by the following equation

$$P = \frac{I_{\sigma^+} - I_{\sigma^-}}{I_{\sigma^+} + I_{\sigma^-}} \quad (2)$$

Here, I_{σ^+} and I_{σ^-} represent the integrated PL intensities detected for the σ^+ and σ^- polarizations. (*R*) and (*S*)-EBAPbI$_3$ films exhibit a similar degree of polarization (∼4%) but reversed signs.

To study the excited state polarization dynamics at low temperatures, we additionally performed CTA measurements on chiral perovskite DMSO−DMF films at 5 K. In comparison to the room temperature TA signals, the GSB2 signals (495−505 nm) for PbI$_2$ heterostructures become more pronounced and show longer lifetimes up to a few ns (Figure S19). Similar to the low-temperature CPL measurements, large polarization in the TA signals for σ^+ and σ^- probes was found at the GSB2 regions (Figure 5h). The polarization of the GSB2 signal only decays after ∼1 ns (Figure S20), which explains the large degree of CPL at cryogenic temperatures. However, because the GSB2 signals live beyond the end of our temporal detection range and coexist with time-dependent broad PIA signals, it is difficult to isolate the GSB2 signal at low temperatures and to fit its decay kinetics. Therefore, as an alternative, we choose a PIA region (PIA2, 475−485 nm), which is located next to GSB2, to extract the polarization kinetics. Figure 5i shows the degree of polarization from the CTA signal (blue line), calculated according to eq 2, with I_{σ^+} and I_{σ^-} given by the TA intensity obtained for probe pulses with σ^+ and σ^- polarization (red and black lines, respectively). The difference between σ^+ and σ^- probes increases from 1 to 4 ps, and stabilizes from 4 ps to hundreds of ps, reaching a high polarization degree of ∼0.2. The rise in polarization kinetics strongly indicates the efficient transfer of chiral excited states from 1D chiral perovskite to a long-lived polarized state in PbI$_2$ nanodomains. The polarization decreases after ∼300 ps. Taken together, these results highlight the significant potential of chiral perovskite/PbI$_2$ heterostructure films for enabling controllable chirality transfer and circularly polarized emission.

Prior work on chiral perovskites has reported heterostructures and their applications for CPL generation and detection.[59−64] Spin funneling in chiral 2D/3D perovskite heterojunctions was studied, and rapid spin transfer from chiral 2D to 3D perovskite was reported, which results in the bright CPL in 3D phases.[60] Yet, the crucial question how alignment of crystal orientations between heterostructures affects transfer of chiral excited states has not been studied. Our work focuses on revealing the detailed mechanisms of chirality transfer in chiral 1D perovskite/PbI$_2$ heterostructures, which underpin CPL generation in chiral 1D heterostructures. Further, based on such orientation-driven chirality transfer methods, we extend this chiral perovskite/PbI$_2$ system, which shows a weak photoluminescence quantum yield (PLQY) value of ∼0.02% at room temperature, to bright chiral perovskite/QDs heterostructures. We spin coated a layer of highly luminescent CdSe/ZnS quantum dots (QDs, PL at 540 nm) as acceptors on top of the chiral 1D perovskites with in-plane (002) facets (DMSO−DMF samples). The obtained chiral 1D perovskite/QDs heterostructures show a high PLQE of ∼50% at room temperature. By efficient chirality funnels within the first ps, the polarized carriers were successfully transferred into QDs layers, resulting in bright CPL signals (gCPL = ∼1.4%) at room temperature (Figure S21). Our results reveal how crystal phase alignment controls photophysical mechanisms for efficient transfer of excited chiral states and provides guidelines for optimizing orientation-driven chiral excitation funneling in the broader class of chiral perovskite film heterostructures.

CONCLUSIONS

In summary, we demonstrate the synthesis of new low-dimensional chiral perovskite (*R*/*S*)-EBAPbI$_3$ single crystals, with single crystal XRD measurements proving that their crystal structures belong to Sohncke space groups. Furthermore, we show that these crystal structures can be transferred to thin film form via dissolution of single crystals in solvents followed by spin coating. In situ XRD and GIWAXS measurements indicate that the solvents used for the spin-coating process can change the crystal orientations in chiral perovskite films, which enables control of both absorption and CD signals of chiral 1D perovskite films. Transient optical spectroscopy measurements confirm that by simply tuning the solvents used for spin-coating, we can drive fast and effective polarized carrier transfer from chiral perovskite phases to PbI$_2$ heterostructures, giving rise to a long-lived polarized excited state with circularly polarized emission at low temperatures. Our demonstration of chiral perovskite heterostructures with controllable chirality transfer provides a new avenue for circularly polarized light generation, broadening the material ranges for future nonlinear optoelectronics and spintronics applications.

MATERIALS AND METHODS

Materials. (*R*)-(+)-α-Ethylbenzylamine, (*S*)-(−)-α-ethylbenzylamine ((*R*/*S*)-EBA), lead oxide (PbO), hydroiodic acid (HI, ≥47%), dimethyl sulfoxide (DMSO, anhydrous) and *N*,*N*-dimethylformamide (DMF, anhydrous) were obtained from Sigma-Aldrich and were used directly without further purification.

Fabrication of Chiral Perovskite Single Crystals and Thin Films. The chiral perovskite single crystals were prepared by hydrothermal synthesis. For a general process, 200 mg PbO and 200 μL (*R*/*S*)-EBA were separately dissolved in 6 mL HI solutions at 95 °C. The resulting solutions were transferred to 25 mL autoclaves and kept at the same temperature (95 °C) inside the oven for 24 h. After slowly decreasing the temperature to room temperature at a rate of 1 °C/h, large needle-shaped single crystals appeared at the bottom

of the autoclaves. Diethyl ether was used to clean the obtained crystals three times, after which they were dried under vacuum conditions. The crystals were stored inside a N_2 filled glovebox before usage.

The thin film fabrication process was performed inside a glovebox under inert gas. The stock solution was prepared by mixing single crystal samples (80 mg) in 400 μL pure DMF, DMSO, or 1:1 mixed DMSO−DMF solutions. After fully dissolving the single crystals at 100 °C, 90 μL of the solutions were spin-coated on 20 × 20 mm precleaned glass substrates (4000 rpm, 35 s). The films were then annealed at 100 °C for 10 min and then stored within a glovebox before characterization.

General Structural and Optical Measurements. In situ XRD measurements were performed at beamline 12.3.2 at the Advanced Light Source at Lawrence Berkeley National Laboratory utilizing a customized spin-coating setup. For such measurements, the sample was placed at an incident angle of 1° in the X-ray beam and the signal was recorded utilizing a DECTRIS Pilatus 1 M X-ray detector placed at 35° relative to the sample. Images were recorded with an exposure time of 1 s. To avoid oxidation effects during the measurement, the sample chamber was constantly purged with nitrogen. The experiments were conducted at a beam energy of 10 keV, corresponding to a wavelength of 1.2398 Å. However, to allow for an easy comparison with steady-state XRD data, the reflections displayed in this work were recalculated to match the wavelength of Cu Kα1 radiation.

The GIWAXS measurements were performed at Beamline PO3 at Deutsches Elektronen-Synchrotron (DESY, Hamburg) under an incidence angle of 0.4° with an X-ray beam energy of 11.87 keV. The data were recorded with an exposure time of 1 s on a Lambda 9 M detector (X-Spectrum). The reshaped GIWAXS, index, and line cuts of scattering data were performed with the python tool INSIGHT.[65] Single crystal XRD measurements were performed on a Bruker D8 Venture system with Mo radiation (λ = 0.71073 Å) at 100 K, for further details see the Supporting Information.

AFM measurements were performed in tapping mode with the commercial AFM (Neaspec, Attocube GmbH). The PtIr alloy-coated silicon tips were driven near their resonance frequency of 280 kHz with the free tapping amplitude of ∼70 nm. Absorption and CD measurements were performed on a commercial CD spectrometer (JASCO J-1700).

PL Measurements. Room-temperature PL measurements were conducted using a home-built setup. A Yb:YAG laser system (Light Conversion Pharos) with an optical parametric amplifier (Light Conversion Orpheus) was used to provide suitable excitation, with wavelengths indicated in the main text. The ICCD camera (Andor, iStar) was used to acquire the PL signals. For low-temperature PL measurements, a Montana cryostation was used to cool down the samples to ∼5 K. For CPL measurements, an additional quarter waveplate and a linear polarizer were placed in front of the camera to control the detection polarizations. TCSPC measurements were performed using a PicoQuant PDL 800-D excitation laser (405 nm) and a Horiba iHR 550 spectrometer. A constant fraction discriminator (PicoQuant PicoHarp 300) and a single-photon avalanche photodiode detector (Micro Photon Devices PD-100-CTE) were used to collect PL signals.

TA Spectroscopy Measurements. Room-temperature TA measurements were performed using a commercial TA setup (Ultrafast Systems, HELIOS). An additional linear polarizer and quarter waveplate were placed in front of the samples to change the polarization of the probe beam for CTA measurements. Low-temperature TA measurements were performed using a home-built setup using the same Montana cryostation that was used for PL measurements. Pump and probed beams were generated with a LightConversion Pharos with an optical parametric amplifier (Light Conversion, Orpheus) producing 270 fs pulses (5 kHz repetition rate, 780 nm). After splitting this output with a beam splitter, one portion of the beam was directed through a CaF_2 crystal window to generate a white light probe (390−780 nm). The other portion of the beam was passed through a linear translation stage (Newport DLS325) and a BBO crystal to provide a 390 nm pump beam. The pump beam was then chopped and overlapped with the probe on the sample. The probe beam was finally collected by an Andor Kymera 193i spectrometer and Andor Zyla 5.5 sCMOS camera. Similar to the room temperature CTA, a linear polarizer and quarter waveplate were used to obtain low-temperature CTA signals.

Accession Codes

Deposition Numbers 2402238 and 2402411 contain the supplementary crystallographic data for this paper. These data can be obtained free of charge via the joint Cambridge Crystallographic Data Centre (CCDC) and Fachinformationszentrum Karlsruhe AccessStructuresservice.

AUTHOR INFORMATION

Corresponding Authors

Shangpu Liu − *Physikalisch-Chemisches Institut, Universität Heidelberg, 69120 Heidelberg, Germany; Walter Schottky Institute and Department of Physics, TUM School of Natural Sciences, Technical University of Munich, 85748 Garching, Germany; Institute of Microstructure Technology, Karlsruhe Institute of Technology, 76344 Eggenstein-Leopoldshafen, Germany; Light Technology Institute, Karlsruhe Institute of Technology, 76131 Karlsruhe, Germany;* orcid.org/0000-0001-9067-7098; Email: shangpu.liu@kit.edu

Felix Deschler − *Physikalisch-Chemisches Institut, Universität Heidelberg, 69120 Heidelberg, Germany*; Email: deschler@uni-heidelberg.de

Authors

Jonathan Zerhoch − *Physikalisch-Chemisches Institut, Universität Heidelberg, 69120 Heidelberg, Germany; Walter Schottky Institute and Department of Physics, TUM School of Natural Sciences, Technical University of Munich, 85748 Garching, Germany;* orcid.org/0000-0003-4336-8828

Markus W. Heindl − *Physikalisch-Chemisches Institut, Universität Heidelberg, 69120 Heidelberg, Germany; Walter Schottky Institute and Department of Physics, TUM School of Natural Sciences, Technical University of Munich, 85748 Garching, Germany;* orcid.org/0000-0001-7968-617X

Chaoran Zhang − *Physikalisch-Chemisches Institut, Universität Heidelberg, 69120 Heidelberg, Germany; Department of Chemistry, National University of Singapore, 117543 Singapore, Singapore; Chemistry Department, TUM School of Natural Sciences, Technical University of Munich, 85748 Garching, Germany*

Tim Kodalle − *Molecular Foundry, Lawrence Berkeley National Laboratory, Berkeley, California 94720, United States;* orcid.org/0000-0002-8792-9669

Kun Sun − *Chair for Functional Materials, Department of Physics, TUM School of Natural Sciences, Technical*

University of Munich, 85748 Garching, Germany; orcid.org/0000-0001-8960-0798

Andrii Shcherbakov – *Physikalisch-Chemisches Institut, Universität Heidelberg, 69120 Heidelberg, Germany; Walter Schottky Institute and Department of Physics, TUM School of Natural Sciences, Technical University of Munich, 85748 Garching, Germany;* orcid.org/0000-0003-4090-4082

Stanislav Bodnar – *Physikalisch-Chemisches Institut, Universität Heidelberg, 69120 Heidelberg, Germany*

Milon Miah – *Physikalisch-Chemisches Institut, Universität Heidelberg, 69120 Heidelberg, Germany*

Mohammad Gholipoor – *Institute of Microstructure Technology, Karlsruhe Institute of Technology, 76344 Eggenstein-Leopoldshafen, Germany; Light Technology Institute, Karlsruhe Institute of Technology, 76131 Karlsruhe, Germany*

Christian Jandl – *Chemistry Department, TUM School of Natural Sciences, Technical University of Munich, 85748 Garching, Germany; Catalysis Research Center, Technical University of Munich, 85748 Garching, Germany*

Alexander Pöthig – *Chemistry Department, TUM School of Natural Sciences, Technical University of Munich, 85748 Garching, Germany; Catalysis Research Center, Technical University of Munich, 85748 Garching, Germany;* orcid.org/0000-0003-4663-3949

Joachim Ballmann – *Anorganisch-Chemisches Institut, Universität Heidelberg, 69120 Heidelberg, Germany;* orcid.org/0000-0001-6431-4197

Ian D. Sharp – *Walter Schottky Institute and Department of Physics, TUM School of Natural Sciences, Technical University of Munich, 85748 Garching, Germany;* orcid.org/0000-0001-5238-7487

Peter Müller-Buschbaum – *Chair for Functional Materials, Department of Physics, TUM School of Natural Sciences, Technical University of Munich, 85748 Garching, Germany;* orcid.org/0000-0002-9566-6088

Carolin M. Sutter-Fella – *Molecular Foundry, Lawrence Berkeley National Laboratory, Berkeley, California 94720, United States;* orcid.org/0000-0002-7769-0869

Ulrich W. Paetzold – *Institute of Microstructure Technology, Karlsruhe Institute of Technology, 76344 Eggenstein-Leopoldshafen, Germany; Light Technology Institute, Karlsruhe Institute of Technology, 76131 Karlsruhe, Germany;* orcid.org/0000-0002-1557-8361

Funding

This project has received funding from the European Research Council (ERC Starting Grant agreement no. 852084—TWIST). P.M.-B. thanks Deutsche Forschungsgemeinschaft (DFG) for financial support via the International Research Training Group 2022 the Alberta/Technical University of Munich International Graduate School for Environmentally Responsible Functional Materials (ATUMS) and under Germany's Excellence Strategy – EXC 2089/1 – 390776260 (e-conversion) as well as from TUM.solar in the context of the Bavarian Collaborative Research Project Solar Technologies Go Hybrid (SolTech). S.L. and K.S. acknowledge the financial support from the China Scholarship Council (CSC). M. W. H., C. M. S.-F. and F.D. recognize the support of the Bavaria California Technology Center (BaCaTec Foerderprojekt Nr 11 [2020–02]).

Notes

The authors declare no competing financial interest.

ACKNOWLEDGMENTS

This research used resources of the Advanced Light Source, which is a DOE Office of Science User Facility under contract no. DE-AC02-05CH11231. Specifically, Beamline 12.3.2 was used. The authors would further like to thank Dr. Nobumichi Tamura for his on-site support at the ALS and for the provision of data processing software. Work at the Molecular Foundry was supported by the Office of Science, Office of Basic Energy Sciences, of the U.S. Department of Energy under Contract no. DE-AC02-05CH11231. We thank Dr. Matthias Schwarzkopf for the help at Beamline PO3, Desy. The static GIWAXS measurement was done at the light source PETRA III AT DESY, a member of the Helmholtz Association (HGF). We thank Dr. Raphael Moral for the discussion and analysis on XRD data.

REFERENCES

(1) Kim, Y.-H.; Zhai, Y.; Lu, H.; Pan, X.; Xiao, C.; Gaulding, E. A.; Harvey, S. P.; Berry, J. J.; Vardeny, Z. V.; Luther, J. M.; Beard, M. C. Chiral-Induced Spin Selectivity Enables a Room-Temperature Spin Light-Emitting Diode. *Science* **2021**, *371*, 1129–1133.

(2) Kim, J. S.; Heo, J. M.; Park, G. S.; Woo, S. J.; Cho, C.; Yun, H. J.; Kim, D. H.; Park, J.; Lee, S. C.; Park, S. H.; Yoon, E.; Greenham, N. C.; Lee, T. W. Ultra-Bright, Efficient and Stable Perovskite Light-Emitting Diodes. *Nature* **2022**, *611*, 688–694.

(3) Chen, C.; Gao, L.; Gao, W.; Ge, C.; Du, X.; Li, Z.; Yang, Y.; Niu, G.; Tang, J. Circularly Polarized Light Detection Using Chiral Hybrid Perovskite. *Nat. Commun.* **2019**, *10*, 1927.

(4) Ishii, A.; Miyasaka, T. Direct Detection of Circular Polarized Light in Helical 1D Perovskite-Based Photodiode. *Sci. Adv.* **2020**, *6*, No. eabd3274.

(5) Yu, D.; Pan, M.; Liu, G.; Jiang, X.; Wen, X.; Li, W.; Chen, S.; Zhou, W.; Wang, H.; Lu, Y.; Ma, M.; Zang, Z.; Cheng, P.; Ji, Q.; Zheng, F.; Ning, Z. Electron-Withdrawing Organic Ligand for High-Efficiency All-Perovskite Tandem Solar Cells. *Nat. Energy* **2024**, *9*, 298–307.

(6) Qin, C.; Sandanayaka, A. S. D.; Zhao, C.; Matsushima, T.; Zhang, D.; Fujihara, T.; Adachi, C. Stable Room-Temperature Continuous-Wave Lasing in Quasi-2D Perovskite Films. *Nature* **2020**, *585*, 53–57.

(7) Ma, J.; Fang, C.; Chen, C.; Jin, L.; Wang, J.; Wang, S.; Tang, J.; Li, D. Chiral 2D Perovskites with a High Degree of Circularly Polarized Photoluminescence. *ACS Nano* **2019**, *13*, 3659–3665.

(8) Di Nuzzo, D.; Cui, L.; Greenfield, J. L.; Zhao, B.; Friend, R. H.; Meskers, S. C. J. Circularly Polarized Photoluminescence from Chiral Perovskite Thin Films at Room Temperature. *ACS Nano* **2020**, *14*, 7610–7616.

(9) Liu, S.; Kepenekian, M.; Bodnar, S.; Feldmann, S.; Heindl, M. W.; Fehn, N.; Zerhoch, J.; Shcherbakov, A.; Pöthig, A.; Li, Y.; Paetzold, U. W.; Kartouzian, A.; Sharp, I. D.; Katan, C.; Even, J.; Deschler, F. Bright Circularly Polarized Photoluminescence in Chiral Layered Hybrid Lead-Halide Perovskites. *Sci. Adv.* **2023**, *9*, No. eadh5083.

(10) Niu, X.; Zeng, Z.; Wang, Z.; Lu, H.; Sun, B.; Zhang, H. L.; Chen, Y.; Du, Y.; Long, G. The First Chiral Cerium Halide towards Circularly-Polarized Luminescence in the UV Region. *Sci. China: Chem.* **2024**, *67* (6), 1961–1968.

(11) Bai, J.; Wang, H.; Ma, J.; Zhao, Y.; Lu, H.; Zhang, Y.; Gull, S.; Qiao, T.; Qin, W.; Chen, Y.; Jiang, L.; Long, G.; Wu, Y. Wafer-Scale Patterning Integration of Chiral 3D Perovskite Single Crystals toward

High-Performance Full-Stokes Polarimeter. *J. Am. Chem. Soc.* **2024**, *146* (27), 18771−18780.
(12) Yuan, C.; Li, X.; Semin, S.; Feng, Y.; Rasing, T.; Xu, J. Chiral Lead Halide Perovskite Nanowires for Second-Order Nonlinear Optics. *Nano Lett.* **2018**, *18*, 5411−5417.
(13) You, Y. M.; Liao, W. Q.; Zhao, D.; Ye, H. Y.; Zhang, Y.; Zhou, Q.; Niu, X.; Wang, J.; Li, P. F.; Fu, D. W.; Wang, Z.; Gao, S.; Yang, K.; Liu, J. M.; Li, J.; Yan, Y.; Xiong, R. G. An Organic-Inorganic Perovskite Ferroelectric with Large Piezoelectric Response. *Science* **2017**, *357* (6348), 306−309.
(14) Qin, Y.; Gao, F. F.; Qian, S.; Guo, T. M.; Gong, Y. J.; Li, Z. G.; Su, G. D.; Gao, Y.; Li, W.; Jiang, C.; Lu, P.; Bu, X. H. Multifunctional Chiral 2D Lead Halide Perovskites with Circularly Polarized Photoluminescence and Piezoelectric Energy Harvesting Properties. *ACS Nano* **2022**, *16*, 3221−3230.
(15) Wei, Q.; Ning, Z. Chiral Perovskite Spin-Optoelectronics and Spintronics: Toward Judicious Design and Application. *ACS Mater. Lett.* **2021**, *3*, 1266−1275.
(16) Lu, H.; Wang, J.; Xiao, C.; Pan, X.; Chen, X.; Brunecky, R.; Berry, J. J.; Zhu, K.; Beard, M. C.; Vardeny, Z. V. Spin-Dependent Charge Transport through 2D Chiral Hybrid Lead-Iodide Perovskites. *Sci. Adv.* **2019**, *5* (12), No. eaay0571.
(17) Long, G.; Sabatini, R.; Saidaminov, M. I.; Lakhwani, G.; Rasmita, A.; Liu, X.; Sargent, E. H.; Gao, W. Chiral-Perovskite Optoelectronics. *Nat. Rev. Mater.* **2020**, *5* (6), 423−439.
(18) Ahn, J.; Lee, E.; Tan, J.; Yang, W.; Kim, B.; Moon, J. A New Class of Chiral Semiconductors: Chiral-Organic-Molecule-Incorporating Organic-Inorganic Hybrid Perovskites. *Mater. Horiz.* **2017**, *4*, 851−856.
(19) Ma, J.; Wang, H.; Li, D. Recent Progress of Chiral Perovskites: Materials, Synthesis, and Properties. *Adv. Mater.* **2021**, *33*, 2008785.
(20) Georgieva, Z. N.; Bloom, B. P.; Ghosh, S.; Waldeck, D. H. Imprinting Chirality onto the Electronic States of Colloidal Perovskite Nanoplatelets. *Adv. Mater.* **2018**, *30*, 1800097.
(21) Wen, Z.; Lu, R.; Gu, F.; Zheng, K.; Zhang, L.; Jin, H.; Chen, Y.; Wang, S.; Pan, S. Enabling Efficient Blue-Emissive Circularly Polarized Luminescence by in Situ Crafting of Chiral Quasi-2D Perovskite Nanosheets within Polymer Nanofibers. *Adv. Funct. Mater.* **2023**, *33*, 2212095.
(22) Ye, C.; Jiang, J.; Zou, S.; Mi, W.; Xiao, Y. Core-Shell Three-Dimensional Perovskite Nanocrystals with Chiral-Induced Spin Selectivity for Room-Temperature Spin Light-Emitting Diodes. *J. Am. Chem. Soc.* **2022**, *144* (22), 9707−9714.
(23) Liu, S.; Heindl, M. W.; Fehn, N.; Caicedo-Dávila, S.; Eyre, L.; Kronawitter, S. M.; Zerhoch, J.; Bodnar, S.; Shcherbakov, A.; Stadlbauer, A.; Kieslich, G.; Sharp, I. D.; Egger, D. A.; Kartouzian, A.; Deschler, F. Optically Induced Long-Lived Chirality Memory in the Color-Tunable Chiral Lead-Free Semiconductor (R)/(S)-$CHEA_4Bi_2Br_xI_{10-x}$ (X= 0−10). *J. Am. Chem. Soc.* **2022**, *144* (31), 14079−14089.
(24) Long, G.; Jiang, C.; Sabatini, R.; Yang, Z.; Wei, M.; Quan, L. N.; Liang, Q.; Rasmita, A.; Askerka, M.; Walters, G.; Gong, X.; Xing, J.; Wen, X.; Quintero-Bermudez, R.; Yuan, H.; Xing, G.; Wang, X. R.; Song, D.; Voznyy, O.; Zhang, M.; Hoogland, S.; Gao, W.; Xiong, Q.; Sargent, E. H. Spin Control in Reduced-Dimensional Chiral Perovskites. *Nat. Photonics* **2018**, *12* (9), 528−533.
(25) Hu, Y.; Florio, F.; Chen, Z.; Phelan, W. A.; Siegler, M. A.; Zhou, Z.; Guo, Y.; Hawks, R.; Jiang, J.; Feng, J.; Zhang, L.; Wang, B.; Wang, Y.; Gall, D.; Palermo, E. F.; Lu, Z.; Sun, X.; Lu, T.-M.; Zhou, H.; Ren, Y.; Wertz, E.; Sundararaman, R.; Shi, J. A Chiral Switchable Photovoltaic Ferroelectric 1D Perovskite. *Sci. Adv.* **2020**, *6*, No. eaay4213.
(26) Zhang, Z.; Wang, Z.; Sung, H. H. Y.; Williams, I. D.; Yu, Z. G.; Lu, H. Revealing the Intrinsic Chiroptical Activity in Chiral Metal-Halide Semiconductors. *J. Am. Chem. Soc.* **2022**, *144*, 22242−22250.
(27) Jana, M. K.; Song, R.; Xie, Y.; Zhao, R.; Sercel, P. C.; Blum, V.; Mitzi, D. B. Structural Descriptor for Enhanced Spin-Splitting in 2D Hybrid Perovskites. *Nat. Commun.* **2021**, *12*, 4982.
(28) Smith, M. D.; Karunadasa, H. I. White-Light Emission from Layered Halide Perovskites. *Acc. Chem. Res.* **2018**, *51*, 619−627.
(29) Yuan, Z.; Zhou, C.; Tian, Y.; Shu, Y.; Messier, J.; Wang, J. C.; Van De Burgt, L. J.; Kountouriotis, K.; Xin, Y.; Holt, E.; Schanze, K.; Clark, R.; Siegrist, T.; Ma, B. One-Dimensional Organic Lead Halide Perovskites with Efficient Bluish White-Light Emission. *Nat. Commun.* **2017**, *8*, 14051.
(30) Urban, J. M.; Jouaiti, A.; Gruber, N.; Delport, G.; Trippé-Allard, G.; Guillemoles, J. F.; Deleporte, E.; Ferlay, S.; Garrot, D. Using Chiral Ammonium Cations to Modulate the Structure of 1D Hybrid Lead Bromide Perovskites for Linearly Polarized Broadband Light Emission at Room Temperature. *J. Mater. Chem. C* **2022**, *10* (34), 12436−12443.
(31) Zhu, H.; Wang, Q.; Sun, K.; Chen, W.; Tang, J.; Hao, J.; Wang, Z.; Sun, J.; Choy, W. C. H.; Müller-Buschbaum, P.; Sun, X. W.; Wu, D.; Wang, K. Solvent Modulation of Chiral Perovskite Films Enables High Circularly Polarized Luminescence Performance from Chiral Perovskite/Quantum Dot Composites. *ACS Appl. Mater. Interfaces* **2023**, *15*, 9978−9986.
(32) Huang, X.; Wu, B.; Zheng, N. Optimizing Solvent Chemistry for High-Quality Halide Perovskite Films. *Acc. Mater. Res.* **2025**, *6* (6), 40−51.
(33) Zheng, X.; Kong, W.; Wen, J.; Hong, J.; Luo, H.; Xia, R.; Huang, Z.; Luo, X.; Liu, Z.; Li, H.; Sun, H.; Wang, Y.; Liu, C.; Wu, P.; Gao, H.; Li, M.; Bui, A. D.; Mo, Y.; Zhang, X.; Yang, G.; Chen, Y.; Feng, Z.; Nguyen, H. T.; Lin, R.; Li, L.; Gao, J.; Tan, H. Solvent Engineering for Scalable Fabrication of Perovskite/Silicon Tandem Solar Cells in Air. *Nat. Commun.* **2024**, *15*, 4907.
(34) Li, B.; Shi, J.; Lu, J.; Tan, W. L.; Yin, W.; Sun, J.; Jiang, L.; Jones, R. T.; Pigram, P.; McNeill, C. R.; Cheng, Y. B.; Jasieniak, J. J. Facile Deposition of Mesoporous PbI2through DMF:DMSO Solvent Engineering for Sequentially Deposited Metal Halide Perovskites. *ACS Appl. Energy Mater.* **2020**, *3*, 3358−3368.
(35) Jeon, N. J.; Noh, J. H.; Kim, Y. C.; Yang, W. S.; Ryu, S.; Seok, S. Il. Solvent Engineering for High-Performance Inorganic-Organic Hybrid Perovskite Solar Cells. *Nat. Mater.* **2014**, *13*, 897−903.
(36) Zanetta, A.; Larini, V.; Vikram; Toniolo, F.; Vishal, B.; Elmestekawy, K. A.; Du, J.; Scardina, A.; Faini, F.; Pica, G.; Pirota, V.; Pitaro, M.; Marras, S.; Ding, C.; Yildirim, B. K.; Babics, M.; Ugur, E.; Aydin, E.; Ma, C. Q.; Doria, F.; Loi, M. A.; De Bastiani, M.; Herz, L. M.; Portale, G.; De Wolf, S.; Islam, M. S.; Grancini, G. Vertically Oriented Low-Dimensional Perovskites for High-Efficiency Wide Band Gap Perovskite Solar Cells. *Nat. Commun.* **2024**, *15*, 9069.
(37) Schönhofer, A.; Kuball, H.-G.; Puebla, C. Optical Activity of Oriented Molecules. IX. Phenomenological Mueller Matrix Description of Thick Samples and of Optical Elements. *Chem. Phys.* **1983**, *76*, 453−467.
(38) Shindo, Y.; Nakagawa, M.; Ohmi, Y. On the Problems of CD Spectropolarimeters. II: Artifacts in CD Spectrometers. *Appl. Spectrosc.* **1985**, *39*, 860−868.
(39) Albano, G.; Pescitelli, G.; Di Bari, L. Chiroptical Properties in Thin Films of π-Conjugated Systems. *Chem. Rev.* **2020**, *120*, 10145−10243.
(40) Berova, N.; Nakanishi, K.; Woody, R. W. *Circular Dichroism: Principles and*; John Wiley & Sons., 2000.
(41) Heindl, M. W.; Kodalle, T.; Fehn, N.; Reb, L. K.; Liu, S.; Harder, C.; Abdelsamie, M.; Eyre, L.; Sharp, I. D.; Roth, S. V.; Müller-Buschbaum, P.; Kartouzian, A.; Sutter-Fella, C. M.; Deschler, F. Strong Induced Circular Dichroism in a Hybrid Lead-Halide Semiconductor Using Chiral Amino Acids for Crystallite Surface Functionalization. *Adv. Opt. Mater.* **2022**, *10*, 2200204.
(42) Sercel, P. C.; Hautzinger, M. P.; Song, R.; Blum, V.; Beard, M. C. Optical Activity of Chiral Excitons. *Adv. Mater.* **2025**, *37*, 2415901.
(43) Pan, R.; Hu, J.; Tao, S.; Kan, L.; Yu, H.; Wang, K. Impact of Crystal Growth Diversity on Magneto-Photoluminescence and Circular Dichroism in Chiral Lead Halide Perovskites. *J. Mater. Chem. C* **2022**, *10*, 16706.

(44) Liu, J.; Sun, Y.; Zhou, Y.; Zhang, C.; Wang, X.; Wang, L.; Xiao, M. Few-Layer PbI2 Nanoparticle: A 2D Semiconductor with Lateral Quantum Confinement. *J. Phys. Chem. Lett.* **2019**, *10*, 7863−7869.
(45) Zhang, D.; Liu, Y.; He, M.; Zhang, A.; Chen, S.; Tong, Q.; Huang, L.; Zhou, Z.; Zheng, W.; Chen, M.; Braun, K.; Meixner, A. J.; Wang, X.; Pan, A. Room Temperature near Unity Spin Polarization in 2D Van Der Waals Heterostructures. *Nat. Commun.* **2020**, *11*, 4442.
(46) Ismail, R. A.; Mousa, A. M.; Khashan, K. S.; Mohsin, M. H.; Hamid, M. K. Synthesis of PbI2 Nanoparticles by Laser Ablation in Methanol. *J. Mater. Sci.: Mater. Electron.* **2016**, *27*, 10696−10700.
(47) Zhao, L.; Yeh, Y. W.; Tran, N. L.; Wu, F.; Xiao, Z.; Kerner, R. A.; Lin, Y. L.; Scholes, G. D.; Yao, N.; Rand, B. P. In Situ Preparation of Metal Halide Perovskite Nanocrystal Thin Films for Improved Light-Emitting Devices. *ACS Nano* **2017**, *11*, 3957−3964.
(48) Jiang, Y.; Sun, C.; Xu, J.; Li, S.; Cui, M.; Fu, X.; Liu, Y.; Liu, Y.; Wan, H.; Wei, K.; Zhou, T.; Zhang, W.; Yang, Y.; Yang, J.; Qin, C.; Gao, S.; Pan, J.; Liu, Y.; Hoogland, S.; Sargent, E. H.; Chen, J.; Yuan, M. Synthesis-on-Substrate of Quantum Dot Solids. *Nature* **2022**, *612*, 679−684.
(49) Heindl, M. W.; Lichtenegger, M. F.; Kodalle, T.; Liu, S.; Solhtalab, N.; Zerhoch, J.; Shcherbakov, A.; Kivala, M.; Sutter-Fella, C. M.; Urban, A. S.; Deschler, F. Ligand-Induced Crystallization Control in MAPbBr3 Hybrid Perovskites for High Quality Nanostructured Films. *Adv. Opt. Mater.* **2025**, *13*, 2402441.
(50) Gull, S.; Jamil, M. H.; Zhang, X.; KwokLi, H. S. G.; Li, G. Stokes Shift in Inorganic Lead Halide Perovskites: Current Status and Perspective. *ChemistryOpen* **2022**, *11*, No. e202100285.
(51) Feldmann, S.; Macpherson, S.; Senanayak, S. P.; Abdi-Jalebi, M.; Rivett, J. P. H.; Nan, G.; Tainter, G. D.; Doherty, T. A. S.; Frohna, K.; Ringe, E.; Friend, R. H.; Sirringhaus, H.; Saliba, M.; Beljonne, D.; Stranks, S. D.; Deschler, F. Photodoping through Local Charge Carrier Accumulation in Alloyed Hybrid Perovskites for Highly Efficient Luminescence. *Nat. Photonics* **2020**, *14*, 123−128.
(52) Hoye, R. L. Z.; Eyre, L.; Wei, F.; Brivio, F.; Sadhanala, A.; Sun, S.; Li, W.; Zhang, K. H. L.; MacManus-Driscoll, J. L.; Bristowe, P. D.; Friend, R. H.; Cheetham, A. K.; Deschler, F. Fundamental Carrier Lifetime Exceeding 1 Ms in Cs2AgBiBr6 Double Perovskite. *Adv. Mater. Interfaces* **2018**, *5*, 1800464.
(53) Zhang, J.; Zhu, X.; Wang, M.; Hu, B. Establishing Charge-Transfer Excitons in 2D Perovskite Heterostructures. *Nat. Commun.* **2020**, *11*, 2618.
(54) Petrov, A. A.; Ordinartsev, A. A.; Fateev, S. A.; Goodilin, E. A.; Tarasov, A. B. Solubility of Hybrid Halide Perovskites in Dmf and Dmso. *Molecules* **2021**, *26*, 7541.
(55) Huang, P. H.; Wang, Y. H.; Ke, J. C.; Huang, C. J. The Effect of Solvents on the Performance of CH3NH3PbI3 Perovskite Solar Cells. *Energies* **2017**, *10*, 599.
(56) Chen, X.; Lu, H.; Wang, K.; Zhai, Y.; Lunin, V.; Sercel, P. C.; Beard, M. C. Tuning Spin-Polarized Lifetime in Two-Dimensional Metal-Halide Perovskite through Exciton Binding Energy. *J. Am. Chem. Soc.* **2021**, *143* (46), 19438−19445.
(57) Valastro, S.; Gavranovic, S.; Deretzis, I.; Vala, M.; Smecca, E.; La Magna, A.; Alberti, A.; Castkova, K.; Mannino, G. Temperature-Dependent Excitonic Band Gap in Lead-Free Bismuth Halide Low-Dimensional Perovskite Single Crystals. *Adv. Opt. Mater.* **2024**, *12*, 2302397.
(58) Bordas, J.; Davis, E. A. The Excitons at the Band Edge of PbI2. *Solid State Commun.* **1973**, *12*, 717−720.
(59) Zhang, X.; Ye, H.; Liang, L.; Niu, X.; Wu, J.; Luo, J. Direct Detection of Near-Infrared Circularly Polarized Light via Precisely Designed Chiral Perovskite Heterostructures. *ACS Appl. Mater. Interfaces* **2022**, *14*, 36781−36788.
(60) Yao, J.; Wang, Z.; Huang, Y.; Xue, J.; Zhang, D.; Chen, J.; Chen, X.; Dong, S. C.; Lu, H. Efficient Green Spin Light-Emitting Diodes Enabled by Ultrafast Energy- and Spin-Funneling in Chiral Perovskites. *J. Am. Chem. Soc.* **2024**, *146*, 14157−14165.
(61) Liu, T.; Shi, W.; Tang, W.; Liu, Z.; Schroeder, B. C.; Fenwick, O.; Fuchter, M. J. High Responsivity Circular Polarized Light Detectors Based on Quasi Two-Dimensional Chiral Perovskite Films. *ACS Nano* **2022**, *16*, 2682−2689.
(62) Tao, L.; Tang, W.; Yan, M.; Ding, L.; Wei, J.; Wang, L.; Li, L.; Li, L.; Yang, D.; Fang, Y. Construction of Chiral-2D/3D Perovskite Heterojunction Films for Efficient Circularly Polarized Light Detection. *J. Mater. Chem. C* **2023**, *11*, 12392−12399.
(63) Zhan, G.; Zhang, J.; Zhang, L.; Ou, Z.; Yang, H.; Qian, Y.; Zhang, X.; Xing, Z.; Zhang, L.; Li, C.; Zhong, J.; Yuan, J.; Cao, Y.; Zhou, D.; Chen, X.; Ma, H.; Song, X.; Zha, C.; Huang, X.; Wang, J.; Wang, T.; Huang, W.; Wang, L. Stimulating and Manipulating Robust Circularly Polarized Photoluminescence in Achiral Hybrid Perovskites. *Nano Lett.* **2022**, *22*, 3961−3968.
(64) Chen, Y.; Ma, J.; Liu, Z.; Li, J.; Duan, X.; Li, D. Manipulation of Valley Pseudospin by Selective Spin Injection in Chiral Two-Dimensional Perovskite/Monolayer Transition Metal Dichalcogenide Heterostructures. *ACS Nano* **2020**, *14*, 15154−15160.
(65) Reus, M. A.; Reb, L. K.; Weinzierl, A. F.; Weindl, C. L.; Guo, R.; Xiao, T.; Schwartzkopf, M.; Chumakov, A.; Roth, S. V.; Müller-Buschbaum, P. Time-Resolved Orientation and Phase Analysis of Lead Halide Perovskite Film Annealing Probed by in Situ GIWAXS. *Adv. Opt. Mater.* **2022**, *10*, 2102722.